Automated Quantitative Quality Assessment of Printed Microlens Arrays

Maximilian Schambach[1], Qiaoshuang Zhang[2],
Uli Lemmer[2], and Michael Heizmann[1]

[1]Karlsruhe Institute of Technology
Institute of Industrial Information Technology
Hertzstr. 16, 76187 Karlsruhe

[2]Karlsruhe Institute of Technology
Light Technology Institute
Engesserstr. 13, 76187 Karlsruhe

Abstract We propose an automated evaluation pipeline utilizing both bright field light and confocal microscope images as well as multiple quality measures to quantitatively evaluate the quality of printed microlens arrays.

1 Introduction

Computational imaging, combining optical and digital signal processing to extract complex information from captured light, has gained much attention in recent years—ranging from multi-camera arrays and combined depth sensors in consumer electronics such as smart phones to coded snapshot spectral imagers [1] or light field cameras [2] explored in the scientific community. Microlens arrays (MLAs), consisting of a multitude of microscopic lenses which are regularly arranged on top of a transparent substrate, play an important role in computational imaging, most prominently in compact light field cameras in which they are placed in front of the camera's

image sensor to spatially code the incident light's angular dependence.

Conventionally, MLAs are manufactured using lithographic methods such as photoresist thermal reflow [3] and nanoimprint lithography [4]. Recently however, inkjet printing of microscopic optical components such as MLAs has become more feasible and affordable, allowing for fast prototyping and production, overall decreasing prototyping cycles when developing new computational cameras.

MLAs are printed applying the Drop-on-Demand inkjet printing method, where a specific volume of optical ink is jetted from the printer's nozzles to prior-determined spots on the substrate, forming a microlens (ML). Printing a multitude of such lenses, either using multiple nozzles and/or moving the nozzle over the substrate, an MLA is printed lens-by-lens. The geometric and optical quality of both the individual lenses as well as the overall manufactured grid depend strongly on a multitude of parameters such as the surface pretreatment of the substrate, the ink composition, the nozzle voltage applied to the piezoelectric transducer, as well as the movement speed of the nozzle and resolution of the printed pattern. Finetuning and optimizing these parameters is key when printing MLAs. However, evaluation of the printed results is usually done manually by experts which is cumbersome, time consuming, and subjective. For these reasons, an automated quantitative (and thus comparable) quality assessment of such printed MLAs is needed. This automated quantitative process allows to manufacture a multitude of MLA prototypes with systematically chosen printing parameters to optimize the overall quality of the array.

To this end, we propose an automated evaluation pipeline utilizing both bright field light and confocal microscope images of the printed MLAs as well as quality measures that can be used to assess the quality of the individual lenses and the overall MLA.

2 Automated quantitative quality assessment

There are four basic geometric quantities of the MLA that one is interested in: the ML radii and sag heights, as well as the vertical and horizontal spacing of the MLs. Furthermore, detecting defects
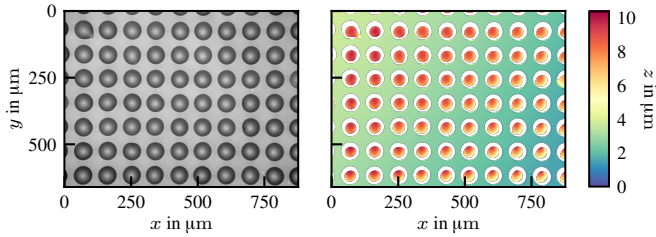
Figure 2.1: Comparison of two typical MLA measurements using a 20x lens. Left: bright field light microscope using reflected light. Right: confocal microscope (missing values are depicted in white).

in the MLA and quantifying the quality of the individual ML's shape are key to the overall assessment of the MLA quality. Finally, the back focal length of the individual MLs has to be measured.

In principle, both confocal microscopes as well as white light interferometers are well suited to measure the geometric properties of MLAs. However, both methods are incapable of providing measurements when the surface inclination is too large which is the case at the ML boundaries. Therefore, a robust measurement of the ML radii and shape is not possible with these methods. Bright field light microscope images (using reflected light) on the other hand are well suited to measure the ML shape because ML boundaries show excellent contrast precisely because of these large surface angles. A comparison of a common MLA light and a confocal measurement is shown in Figure 2.1. To measure the back focal length of the MLs, a transmitted light microscope, using a collimated light source, is well suited.

For this reason, we propose to use both bright field and confocal measurements to measure the MLA properties. Commonly, confocal microscopes offer both bright light and confocal measurements using the same optical path which makes post-capture alignment of the two measurements unnecessary (this is usually not the case for white light interferometers). In our experiments, we use a Leica DCM8 microscope with both a 20x and 50x lens. Using the 20x lens, the microscope has a lateral resolution of 0.645 μm and a vertical resolution of 1 μm whereas with the 50x lens it has a lateral resolution of
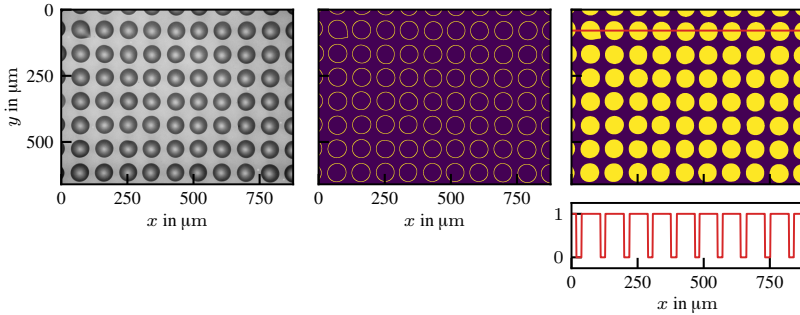
Figure 2.2: Obtaining a rough estimate of the ML radius and spacing using 1D sections of the binary image. Left: original bright field microscope image. Middle: edges detected using the Canny algorithm. Right: filled binary image and 1D section with maximum radius estimate.

0.258 μm and a vertical resolution of 0.1 μm. The MLAs are printed using a PiXDRO LP50 inkjet printer and a 10 pL cartridge. The individual MLs have a diameter of about 50–60 μm with a sag height of approximately 5 μm. Therefore, we use the 20x lens to measure all properties of the MLA except the sag height, for which a higher vertical resolution, using the 50x objective, is needed. Of course, depending on the MLAs under consideration, the chosen lenses may deviate from ours.

For each MLA a multitude of measurements is collected to increase the statistical significance of the evaluation: for the 20x magnification, we use nine confocal and corresponding bright field light microscope measurements, and three confocal and corresponding bright field light microscope measurements using the 50x lens.

2.1 Rough radius and spacing estimate

First, to bootstrap the subsequent property estimates, a rough estimate of the ML radius $\hat{r}_r$ and spacing $\hat{s}_r$ is obtained using a single bright field light microscope image. If multiple measurements have been collected for a single MLA, a random one is chosen. Image edges are detected using the Canny algorithm [5] followed by a filling of closed regions in the edge image. Using several hundred con-
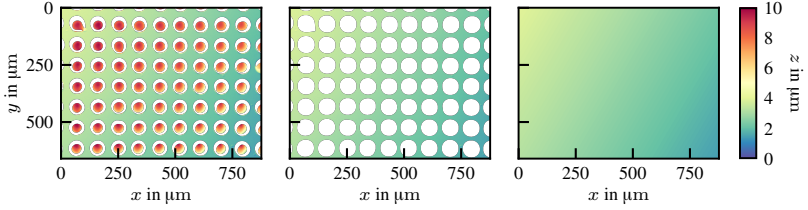
Figure 2.3: Estimating the tilt of the MLA w.r.t. the optical axis. Left: original confocal measurement. Middle: Masked confocal measurement. Right: estimated ideal MLA background plane with estimated tilt $\hat{\vartheta} = 0.09°$.

secutive horizontal 1D sections of the binary image, the radius and spacing are calculated as the maximum median number of succeeding ones (respectively zeros) of each section (compare Figure 2.2). In the case that multiple grid spacings are expected, e. g. for non-square or hexagonal grid layouts, the procedure has to be performed also for the vertical axis.

2.2 Tilt estimate

For measurements using the light microscope, the normal of the MLA and the optical axis of the microscope have to be well aligned. Misalignment leads to perspective distortions of the ideally regular grid. Hence, it will lead to systematic measurement inaccuracies when estimating the ML radius and grid spacing. To validate the MLA alignment, the flat substrate surface (on which the MLs are printed) can be used. The binary image extracted from the light microscope measurement (as described in Section 2.1) is used as a binary mask to mask out the individual MLs in the corresponding confocal measurement. To this end, a threefold binary dilation (using a fully connected 3×3 structuring element) is applied to the binary image to increase the size of the individual ML's mask. The binary mask is then applied to the confocal measurement to extract the substrate surface. Using the extracted surface, the ideal surface plane is estimated via a least-squares approximation of the measurements via the plane equation

$$z = ax + by + c \,, \tag{2.1}$$

55

(a) (b) (c) (d)
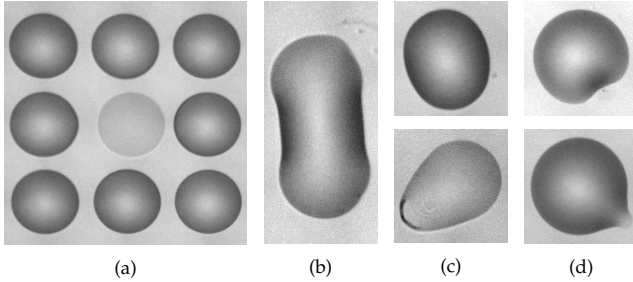
Figure 2.4: Typical shape deviations and defects in printed MLAs. (a) Missing ML. (b) Joint MLs. (c) Global shape deviation. (d) Local shape deviation.

where $\alpha = \arctan a$ and $\beta = \arctan b$ are the plane's intersection angles with the x- and y-axis, respectively. Using the estimated plane's normal vector $\hat{\mathbf{n}} = (\hat{a}, \hat{b}, 1)^{\mathrm{T}}$ and the optical axis $\mathbf{n}_0 = (0, 0, 1)^{\mathrm{T}}$, the MLA tilt angle ϑ is determined as

$$\vartheta = \arccos \langle \hat{\mathbf{n}}, \mathbf{n}_0 \rangle. \tag{2.2}$$

An overview of the procedure is shown in Figure 2.3.

When the estimated tilt is too large, the microscope tilt has to be calibrated using a tilt stage. In our experiment, we use the MLA substrate surface as a reference surface to calibrate the tilt of the MLA to be below $0.1°$, however using a reference calibration mirror is also possible. In principle, when the projection matrix of the microscope is known, the estimated tilt can be used to either de-tilt the light microscope measurements or estimate an upper bound of the further MLA property estimates. However, due to the extremely narrow depth of field, a geometric calibration of the light microscope is extremely challenging.

2.3 Geometric properties estimate

Estimating the geometric properties of the MLA, one faces several challenges: First, defects in the printed MLA have to be robustly detected and taken into account when estimating the underlying regular grid's parameters. Second, the individual MLs may be deformed

and thus not perfectly circular, making the circle detection and radius estimation more difficult. Lastly, the used algorithm should not be too complex to be able to evaluate a multitude of measurements in a reasonable time.

Defects and shape deviations are common in MLA printing, in particular when the printing parameters are non-optimal and/or when the substrate surface is contaminated with dust or other particles. Common defects are missing as well as joint MLs, for which we will propose methods for detection. For the shape deviations, we roughly divide them into two classes: global and local shape deviations. Global shape deviations refer to ML shapes that are overall deviating from a perfect circular shape, for example elliptical MLs, whereas local shape deviations correspond to MLs that are overall circular with localized defects. We will introduce quality measures to quantify both types of shape deviations. For an overview of typical defects and shape deviations in printed MLAs, see Figure 2.4.

In a first step, again the edges are calculated from the light microscope measurement using the Canny algorithm. The detected edges are labeled into individual clusters using a standard labeling algorithm. Each cluster now represents exactly one ML or defect. For each cluster, the bounding box is calculated. If the larger side of the bounding box is larger than 110 % of the estimated rough diameter $2\hat{r}_r$, the cluster is classified as a defect. This robustly detects joint lenses (which typically stretch over $4\hat{r}_r$) as well as leaked MLs. If the larger side of the bounding box is smaller than 90 % of the estimated rough diameter, the cluster is classified as debris, containing all non-geometric defects such as dust, droplets, and scratches.

Second, the individual MLs and their radii are estimated. To this end, we propose a multi-scale extension to the circular Hough transform [6]. Since the deviation of the ML shape from a perfect circle can be quite severe (as shown in Figure 2.4), the Hough transform, applied to the original edge image, may not detect all lenses robustly. Furthermore, the accuracy of the estimated radii is limited to integer pixel values. To overcome these limitations, we perform the Hough transform on several scales $\mathcal{S} = \{s_1, s_2, ..., s_N\}$. To increase robustness against shape deviations, some scales are chosen to be smaller than one; to increase accuracy, the remaining scales are chosen to be larger than one. In our experiments we choose

$\mathcal{S} = \{0.33, 0.5, 1, 1.5, 2\}$. At each scale s_i, the edge image is calculated from the scaled light microscope measurement and the Hough transform is applied to the scaled edge image. To narrow the search space, the size of the accumulation matrix is reduced by limiting the radius range to $(1 \pm 0.1)s_i\hat{r}_r$. The detected center coordinates and radii are collected together with their accumulation score. The number of detected MLs per scale decreases with larger scales: due to the shape deviations, a non-circular shape is robustly detected in the down-scaled image, however it may not reach a large accumulation score in higher scales. Therefore, starting with the lowest scale s_1, for every detected center c_i at scale i, a corresponding center c_{i+1} at the next higher scale is searched. To this end, the center c_i and radius r_i are projected into the higher scale:

$$c_{i \to i+1} = \frac{s_{i+1}}{s_i} c_i, \quad r_{i \to i+1} = \frac{s_{i+1}}{s_i} r_i. \tag{2.3}$$

Using a k-d tree-based nearest neighbor search within a unit ball of the projected radius around the projected center, the higher scale correspondent is determined. If a corresponding center is found at the higher scale, the estimated center and radius are used from that scale, if not, the current radius and center estimates are used. This procedure is repeated iteratively for every scale. The final detected centers and corresponding radii are then filtered: centers that are within a margin of $\hat{r}_r$ of the image border, as well as centers that lie within the bounding box of a detected defect are neglected.

Third, using the detected centers and the initial rough spacing estimate, the grid spacing in x- and y direction is estimated, and missing MLs are detected. To estimate the spacing, following an approach similar to the grid estimation proposed by Dansereau et al. [7], a k-d tree of the final estimated centers is built. Starting with the center closest to the origin, the grid is traversed vertically and horizontally using the rough estimate of the grid basis vectors, $\mathbf{a} = (\hat{s}_r, 0)$, $\mathbf{b} = (0, \hat{s}_r)$, in the case of a square grid. That is, the current center position c_{curr} is updated by adding the corresponding grid basis vector,

$$c_{\text{up, horz}} = c_{\text{curr}} + \mathbf{a}, \quad c_{\text{up, vert}} = c_{\text{curr}} + \mathbf{b}. \tag{2.4}$$
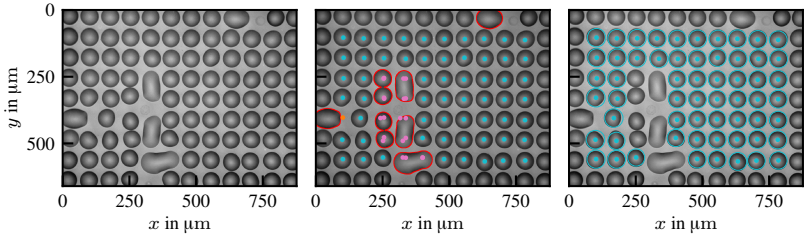
Figure 2.5: Detection results for an MLA with severe defects. Left: original bright field microscope image. Middle: detected centers (cyan), predicted centers (pink), missing MLs (orange), and detected defects (red border). Right: Detected centers and ideal circles with corresponding estimated radius.

If a detected center can be found in the neighborhood around the updated center, the found center is used as the new current center (independently for the horizontal and the vertical traverse) and the distance (vertical or horizontal) to the previous center is measured. If no center can be found, the updated center is marked as a candidate for a missing ML and used as the new current center. Having collected these distances for all MLs and multiple measurements, outliers are removed, using the median and median deviation. For example, missing MLs will lead to measured distances that are twice as large as the correct spacing and are therefore neglected. After the full grid has been traversed horizontally and vertically, the missing ML candidates are further investigated. First, since the two independent traverses may have detected the same candidates, the candidates are filtered such that there is only one unique candidate within the estimated radius. Finally, if a missing ML candidate has at least 2 detected grid neighbors and is not within the bounding box of a previously detected defect, the candidate is counted as a missing ML. An example of the detection result is given in Figure 2.5.

2.4 Microlens quality estimate

Having detected the individual MLs and estimated their radii, the geometric quality of the individual lenses is estimated. In principle, the Hough accumulation scores Q_{acc} could be used to quantify the shape quality, however theses scores are not directly comparable

Table 1: ML quality estimates for perfectly circular (top), globally deviating (middle) and locally deviating (bottom) MLs. Estimated ML centers and ideal circles with estimated radii are depicted in red. Note that the scales of the images are not identical.

ML	$r/\mu m$	$Q_{\text{acc}}/\%$	$Q_{\text{c}}/\%$	$Q_{\text{cdev}}/\%$	Q_{cv}
	33.4	47.02	0.84	0.97	1.15
	33.5	55.91	0.85	1.04	1.23
	32.2	31.43	5.58	6.28	1.13
	30.3	14.46	9.02	11.40	1.26
	34.5	34.87	3.56	6.54	1.84
	33.9	45.72	2.24	3.96	1.77

between different MLAs. For this reason, we propose three shape quality measures. The microlens edges have been previously labeled and clustered. For each ML, the distance d_i from every edge pixel i to the ideal ML circle (using the corresponding estimated center and radius), relative to the estimated radius, is measured. Interpreting the measured distances as realizations of a random variable d, the following measures are defined as the sample mean, sample standard deviation, and sample coefficient of variation, respectively:

$$Q_{\text{c}} = \hat{\mu}_{\text{d}}, \quad Q_{\text{cdev}} = \hat{\sigma}_{\text{d}}, \quad Q_{\text{cv}} = \hat{\sigma}_{\text{d}}/\hat{\mu}_{\text{d}}. \tag{2.5}$$

While Q_{c} quantifies the overall deviation from the ideal circular shape, Q_{cdev} is well suited to measure the localization of the deviation. That is, global shape defects have a lower Q_{cdev} than local shape defects. However, larger mean deviations Q_{c} also in general lead to larger standard deviations Q_{cdev} which makes the values of Q_{cdev} harder to compare directly. Hence, the coefficient of variation Q_{cv} is used. A Q_{cv} close to one corresponds to circular shapes or
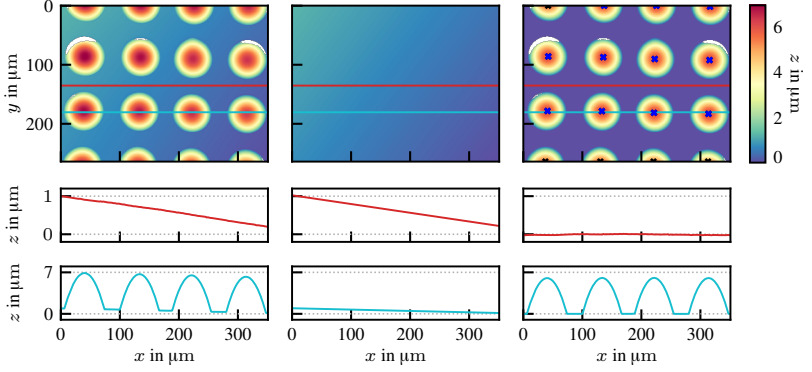
Figure 2.6: ML height estimate. Left: original confocal image. Middle: estimated ideal background plane. Right: de-tilted and zero-leveled confocal measurement with detected local maxima (blue x) and neglected outliers (black x).

shapes with a global shape defect; larger values occur when the defect is more localized. Table 1 shows some example MLs with their corresponding quality measures.

2.5 Sag height estimate

The MLA tilt and ML sag heights are estimated using the confocal and light microscope measurements at 50x magnification. In complete analogy to the procedure presented in Section 2.2 but using the 50x magnification measurements, the tilt ϑ and the offset c of the background surface are estimated. The confocal data points $\mathbf{x} = (x, y, z)$ are then zero-leveled and de-tilted,

$$\tilde{\mathbf{x}} = \mathbf{R_n}(\varphi)(\mathbf{x} - c). \tag{2.6}$$

Here, the rotation matrix $\mathbf{R_n}$ is calculated from the rotation vector $\mathbf{n} = \hat{\mathbf{n}} \times \mathbf{n}_0 / \|\hat{\mathbf{n}} \times \mathbf{n}_0\|$. The individual ML sag heights can then simply be measured using the local maxima in the de-tilted and zero-leveled confocal measurement. To neglect measurements from partially imaged MLs, occuring at the image boundaries, outliers from the measured heights are removed using the median and median
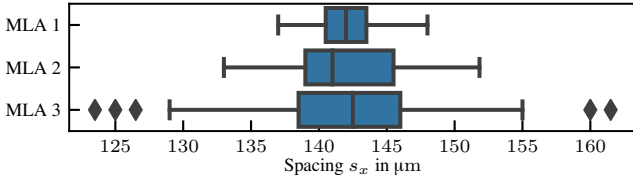
Figure 2.7: Example comparison of the measured grid spacing for three MLAs.

deviation. An example of the measurement results is depicted in Figure 2.6.

2.6 Visualization and comparison

A multitude of measurements is collected for each MLA: the radii, heights, and quality measures are measured for every individual ML, whereas the spacing is calculated pairwise. Hence, a comparison between different MLAs can be performed by either directly comparing mean and/or standard deviation values of the corresponding values or by analyzing the underlying probability distributions in more detail. For this, box or violin plots, in combination with a kernel density estimation of the data, are often used, compare Figure 2.7: while the median values of the measured grid spacings are very similar, the data of *MLA 2* and *MLA 3* are wider spread, corresponding to a less regular grid.

3 Conclusion

We have proposed and analyzed an automated evaluation pipeline utilizing both bright field light and confocal microscope images as well as multiple quality measures to automatically and quantitatively evaluate the quality of printed microlens arrays.

References

1. G. R. Arce, D. J. Brady, L. Carin, H. Arguello, and D. S. Kittle, "Compressive coded aperture spectral imaging: An introduction," *IEEE Signal Processing Magazine*, vol. 31, no. 1, pp. 105–115, 2014.

2. R. Ng, M. Levoy, M. Brédif, G. Duval, M. Horowitz, and P. Hanrahan, "Light field photography with a hand-held plenoptic camera," *Computer Science Technical Report (CSTR)*, vol. 2, no. 11, pp. 1–11, 2005.

3. H. Jung and K.-H. Jeong, "Monolithic polymer microlens arrays with high numerical aperture and high packing density," *ACS Applied Materials & Interfaces*, vol. 7, no. 4, pp. 2160–2165, 2015.

4. C. Peng, X. Liang, Z. Fu, and S. Y. Chou, "High fidelity fabrication of microlens arrays by nanoimprint using conformal mold duplication and low-pressure liquid material curing," *Journal of Vacuum Science & Technology B*, vol. 25, no. 2, pp. 410–414, 2007.

5. J. Canny, "A computational approach to edge detection," *IEEE Transactions on Pattern Analysis and Machine Intelligence*, no. 6, pp. 679–698, 1986.

6. R. O. Duda and P. E. Hart, "Use of the Hough transformation to detect lines and curves in pictures," *Comm. of the ACM*, vol. 15, no. 1, pp. 11–15, 1972.

7. D. G. Dansereau, O. Pizarro, and S. B. Williams, "Decoding, calibration and rectification for lenselet-based plenoptic cameras," in *IEEE Conference on Computer Vision and Pattern Recognition*, 2013, pp. 1027–1034.